





Suppressed-scattering spectral windows for radiative cooling applications

JOSÉ M. PÉREZ-ESCUDERO,¹ ALICIA E. TORRES-GARCÍA,¹
CARLOS LEZAUN,¹ ANTONIO CAGGIANO,² IGNACIO PERALTA,^{3,4,5}
JORGE S. DOLADO,^{6,7} MIGUEL BERUETE,¹  AND IÑIGO
LIBERAL^{1,*} 

¹Department of Electrical, Electronic and Communications Engineering, Institute of Smart Cities (ISC), Public University of Navarre (UPNA), 31006 Pamplona, Spain

²DICCA, Dept. of Civil, Chemical and Environmental Engineering, University of Genova, Via Montallegro 1, Genova 16145, Italy

³Institut für Werkstoffe im Bauwesen, Technische Universität Darmstadt, Germany

⁴Centro de Investigación de Métodos Computacionales (CIMEC), Universidad Nacional del Litoral (UNL)/ Consejo Nacional de Investigaciones Científicas y Técnicas (CONICET), Predio CONICET “Dr. Alberto Cassano”, Colectora Ruta Nac. 168 km 0, Paraje El Pozo, 3000 Santa Fe, Argentina

⁵Laboratorio de Flujiometría (FLOW), Facultad Regional Santa Fe (FRSF), Universidad Tecnológica Nacional (UTN), Lavaise 610, 3000 Santa Fe, Argentina

⁶Centro de Física de Materiales CFM (CSIC-UPV/EHU), Donostia-San Sebastián, Spain

⁷Donostia International Physics Center (DIPC), Donostia-San Sebastián, Spain

*inigo.liberal@unavarra.es

Abstract: The scattering of light by resonant nanoparticles is a key process for enhancing the solar reflectance in daylight radiative cooling. Here, we investigate the impact of material dispersion on the scattering performance of popular nanoparticles for radiative cooling applications. We show that, due to material dispersion, nanoparticles with a qualitatively similar response at visible frequencies exhibit fundamentally different scattering properties at infrared frequencies. It is found that dispersive nanoparticles exhibit suppressed-scattering windows, allowing for selective thermal emission within a highly reflective sample. The existence of suppressed-scattering windows solely depends on material dispersion, and they appear pinned to the same wavelength even in random composite materials and periodic metasurfaces. Finally, we investigate calcium-silicate-hydrate (CSH), the main phase of concrete, as an example of a dispersive host, illustrating that the co-design of nanoparticles and host allows for tuning of the suppressed-scattering windows. Our results indicate that controlled nanoporosities would enable concrete with daylight passive radiative cooling capabilities.

© 2023 Optica Publishing Group under the terms of the [Optica Open Access Publishing Agreement](#)

1. Introduction

Radiative cooling has emerged as a passive technology with the potential for a major reduction of energy consumption. It promises to cut the costs of cooling systems, alleviate the urban island effect, and combat global warming [1–4]. In essence, passive radiative cooling takes advantage of thermal emission to transmit energy through the atmospheric transparency window, using outer space as a cold sink. Achieving daytime and passive radiative cooling poses the additional technological challenge of minimizing sunlight absorption, while simultaneously maintaining a high infrared emissivity in the atmospheric transparency window (see Fig. 1).

However, this challenge can be met by nanophotonic design. The seminal work by Raman et al. [5] demonstrated that nanophotonic multilayered structures make passive daytime radiative cooling possible. Since then, multilayered [6–10] and more advanced metamaterial structures [11,12] have been actively investigated. While nanophotonic engineering provides an excellent

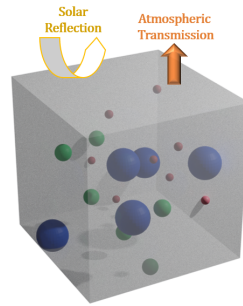


Fig. 1. Sketch of a radiative cooling composite material, consisting of a mixture of resonant nanoparticles reflecting solar light while efficiently radiating heat through the atmospheric window.

radiative cooling performance, the need to rely on complex nanofabrication processes and expensive materials limits its large-scale and low-cost deployment. Composite materials provide an alternative approach towards daytime passive radiative cooling without the need of nanofabrication process and/or expensive materials. Instead, composite materials use random mixtures of nanoparticles, whose size distribution is engineered to support the resonances needed for efficient solar reflectance. This concept has proven to be very successful, leading to cost-effective solutions for radiative cooling structures in the form of microsphere coatings and paints [13–17], polymers [18–21], biomimetics [22,23], textiles [24,25] and structural materials like wood [26].

The nanophotonic design of composite materials for radiative cooling has predominantly focused on the use of Mie scattering resonances to enhance solar reflectance. However, scattering theory is a large and mature field, and many of the ideas developed through years of research can be applied to the design of radiative cooling systems. Indeed, the interplay between material dispersion and geometry enables a wealth of scattering phenomena including resonantly enhanced scattering and absorption processes [27–29], scattering cancellation and invisibility [30], superdirectivity [31,32], cloaked (minimum scattering) sensors [33,34], superbackscattering [35–37], frequency comb scattering [38], Fano resonances [39], nonradiating epsilon-near-zero [40–42] and anapole [43] modes, as well as the enhancement [44,45] and inhibition [46–48] of the radiation by quantum emitters. The large body of work on scattering theory suggests that the interplay between dispersion and geometry should be carefully examined when choosing a material system for radiative cooling applications. Following this motivation, here we analyze the impact of material dispersion on the scattering performance of nanoparticles that are commonly employed to enhance the solar reflectance of radiative cooling systems. As we will show, several of them exhibit “suppressed-scattering windows” (i.e., the suppression of scattering for a wide range of nanoparticle radii) overlapping with the atmospheric transparency window, providing a key insight in the design of composite materials for daytime passive radiative cooling.

2. Scattering from dispersive nanoparticles

We start by analyzing the individual scattering performance of popular nanoparticles used in radiative cooling applications. As case studies, we consider titanium dioxide (TiO_2), alumina (Al_2O_3) and silica (SiO_2) nanoparticles, which are commonly employed for increasing the solar reflectance [49,50]. For comparison, we include in the analysis nanoparticles made of an ideally nondispersive material, with dielectric constant $\epsilon_{ND} = 2$ at all frequencies. Figure 2(a) depicts the frequency dispersion of their permittivities following tabulated data (see Methods: Material parameters). It can be concluded from the figure that, at visible frequencies, all materials behave

approximately as nondispersive dielectrics with negligible loss. Therefore, their frequency response in this range is qualitatively similar, the main difference being their dielectric constant value. For example, $\epsilon_{ND} = 2$, $\epsilon_{TiO_2} = 6.17$, $\epsilon_{Al_2O_3} \approx 3.05$, and $\epsilon_{SiO_2} = 2.10$, at $\lambda = 1 \mu\text{m}$, with TiO_2 exhibiting a significantly larger value. Therefore, all studied materials are expected to support dielectric (Mie-scattering) resonances in the visible, enhancing the solar reflectance. It justifies their choice as popular materials for radiative cooling applications. By contrast, their material response at infrared frequencies presents a more involved resonant response, raising qualitative differences between the materials. For example, while Al_2O_3 is characterized by relatively sharp material resonances at frequencies below the atmospheric window, TiO_2 exhibits a broad resonance band at those wavelengths. As for SiO_2 , it features a sharp resonant peak within the atmospheric window. Therefore, the scattering performance of these materials is expected to be very different at infrared frequencies, highlighting the need to take into account material dispersion for their implementation within radiative cooling systems.

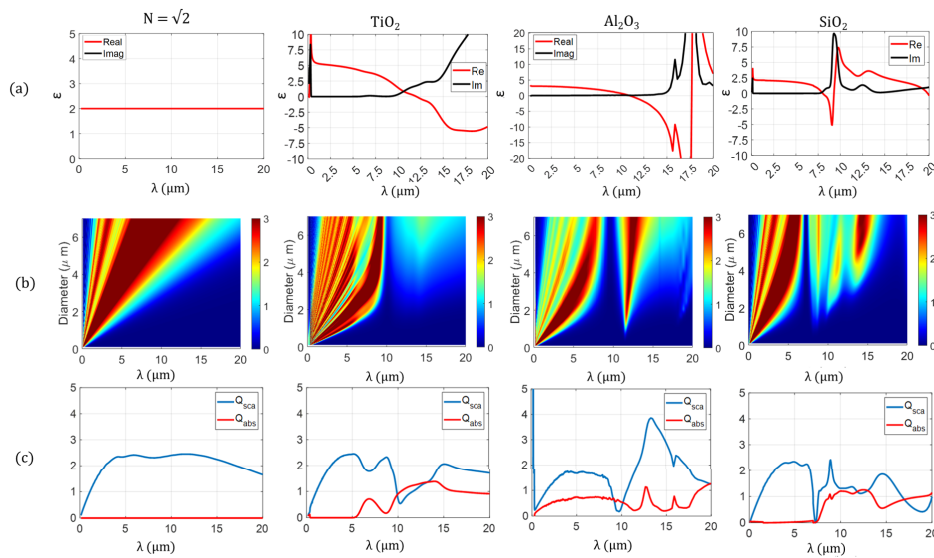


Fig. 2. Scattering efficiency calculations for nondispersive dielectric, titanium dioxide (TiO_2), alumina (Al_2O_3), and silica (SiO_2) nanoparticles: (a) Frequency dispersion of the complex permittivity. Real part shown in solid red line and imaginary part in solid black line. (b) Scattering efficiency for the nanoparticles embedded in air ($\epsilon_h = 1$). (c) Average value of the scattering and absorption efficiencies for nanoparticle radii ranging from 0 to $7 \mu\text{m}$.

Figure 2(b) depicts the scattering efficiency of nanoparticles made of these materials as a function of wavelength and nanoparticle radius, computed by using Mie-scattering theory (see Methods: Calculation of the scattering efficiency). For the nondispersive dielectric material, the scattering efficiency exhibits multiple resonant peaks with a linear dispersion in wavelength and nanoparticle size. Within the $0.2 - 2.0 \mu\text{m}$ frequency band, a qualitatively similar behavior is obtained for TiO_2 , Al_2O_3 and SiO_2 nanoparticles. Thus, it is confirmed that in this frequency range these materials effectively behave as nondispersive dielectrics. Minor differences arise due to the higher value of the TiO_2 dielectric constant, yielding more densely packed resonances, and with higher peak values.

By contrast, the impact of material dispersion in the scattering performance is more crucial at infrared frequencies. Due to material dispersion, the nanoparticle resonances exhibit a highly nonlinear dispersion. In addition, the scattering efficiency maps reveal several frequency bands where the scattering efficiency is suppressed for all considered nanoparticle radii. Comparison

with Fig. 2(a) reveals that these minima correspond to frequencies ω_1 where the real part of the permittivity approximately equals one, i.e., $\epsilon(\omega_1) \approx 1$ with negligible loss. More generally, when the dielectric permittivity of the nanoparticle matches that of its host matrix, the scattered field becomes identically zero, irrespectively of the size and shape of the nanoparticle. Therefore, the scattering is minimized for any nanoparticle radius, forming a “suppressed scattering window”. While the origin of such suppressed-scattering window is conceptually simple, we believe that their important technological implications, with realistic materials, and for radiative cooling applications, has not been fully explored. As we will show, it should critically condition the choice of the nanoparticle material.

Remarkably, the suppressed-scattering windows of known nanoparticles such as TiO_2 and Al_2O_3 overlap with the atmospheric transparency window. Therefore, nanoparticle systems based on TiO_2 and Al_2O_3 will exhibit a transparency band where thermal emission is needed the most. This property facilitates the design of selective thermal emitters for radiative cooling applications. For example, if a material is a good thermal emitter but has poor solar reflectance, one could add a layer of these nanoparticles on top of it, increasing its solar reflectance while guaranteeing that the suppressed scattering window allows for thermal emission within that frequency band. Alternatively, one could add nanoparticles within a good thermal emitter. Selecting nanoparticles whose permittivity match that of the host in the atmospheric window one could again increase the solar reflectance, while minimizing the impact on the thermal emission performance. On the contrary, SiO_2 nanoparticles exhibit strong resonances within the atmospheric window, which will result in undesired reflectivity for absorption in a bulky material. At the same time, nanoparticle resonances enhance the absorption of poor thermal emitters, particularly if it has a small volume. For this reason, SiO_2 are a good design strategy for thin and electrically small radiative coolers [17], or for cases when the matrix itself is a poor thermal emitter. These conclusions highlight that the dispersion profile of resonant nanoparticles must be carefully taken into account, as different profiles lead to different strategies in the design of radiative coolers. Specifically, materials with suppressed-scattering spectral windows are desired for bulky devices, where absorption can be achieved in a large volume as long as the reflectivity is minimized. On the other hand, nanoparticles with resonances in the visible are preferable for thin-film configurations, where one has to rely on resonances to achieve large absorption within a small volume.

To further illustrate this point, Fig. 2(c) depicts the average scattering efficiency for nanoparticle radii ranging from 0 to 7 μm . The results illustrate the presence of the suppressed-scattering window for any nanoparticle radii, and the different scattering performance of TiO_2 , Al_2O_3 and SiO_2 at infrared frequencies. For the sake of completeness, Fig. 2(c) also includes the average absorption efficiency. It can be concluded from the figure that that the absorption in the solar window is negligible for all materials except the Al_2O_3 , which might limit its solar reflectance. By contrast, in the atmospheric window, the absorption is significant for all TiO_2 , Al_2O_3 and SiO_2 , supporting the conclusion that that these materials are useful for reflecting the solar irradiance due to scattering while they are still good emitter in the atmospheric window.

3. Reflection from random mixtures of nanoparticles

Radiative cooling systems augmented with resonant nanoparticles typically consist of complex composite materials, containing distributions of nanoparticles of different sizes in a random arrangement. Moreover, the size of resonant nanoparticles is comparable to, or larger than, the wavelength of operation, posing additional difficulties on the theoretical modelling. Therefore, providing an accurate estimation of the radiative cooling performance of a composite material containing densely packed resonant nanoparticles is a cumbersome task. Predicting accurately both the net emitter power and the cooling rate of a composite material requires large-scale and stochastic full-wave numerical simulations. However, an approximate estimation can be obtained with the use of effective medium theories (EMTs) [51], where extensions to conventional

EMTs allow for the analysis of composites containing large and resonant particles [52–54]. In this section, we use these approximate methods to conceptually validate the extension of the conclusions drawn in the previous section to random mixtures of nanoparticles.

Figure 3 depicts the reflectivity $R = \left| \frac{1 - \sqrt{\epsilon_e/\mu_e}}{1 + \sqrt{\epsilon_e/\mu_e}} \right|^2$ from composites containing a distribution of resonant nanoparticles, modeled with effective permittivity (ϵ_e) and permeability (μ_e), calculated via generalized Maxwell-Garnett theories (see Methods: Calculation of the reflectivity from composite materials). It is considered a host large enough to avoid any transmission, therefore the incident wave is either reflected or absorbed. Following the analysis of the scattering of individual nanoparticles, we consider mixtures of nanoparticles made of the same four materials, all immersed in a transparent, unit-permittivity host. For all four classes of mixtures, we consider a distribution of nanoparticle sizes from 50nm to 300nm with a step of 50nm, which is a smaller range size of particle regarding to the analysis performed previously, since it is selected to achieve a high reflectivity within the solar spectrum window. In all four cases, we study mixtures with three different filling factors of 10%, 35% and 70%, which is defined as the volume fraction occupied by the scattering nanoparticles. We note that the EMT takes into account the interaction between the nanoparticles, and the results might in principle deviate from those of the analysis of individual nanoparticles, particularly for large filling factors. However, the results reported in Fig. 3 qualitatively match the conclusions drawn in Section 2. Specifically, it is found that the reflectivity spectra for the nondispersive nanoparticles remain flat, showing no particular resonances. On the other hand, dispersive nanoparticle materials, like TiO_2 , Al_2O_3 and SiO_2 , feature a clear reflectivity dip, whose wavelength exactly corresponds to the suppressed-scattering window observed at the individual nanoparticle level (see Fig. 2). In fact, the reflectivity dip remains fixed at the same wavelength even for large filling factors, for which the reflectivity in the rest of the spectrum is high. Hence, it is confirmed that the interaction between the nanoparticles does not affect the existence and location of the reflectivity minima.

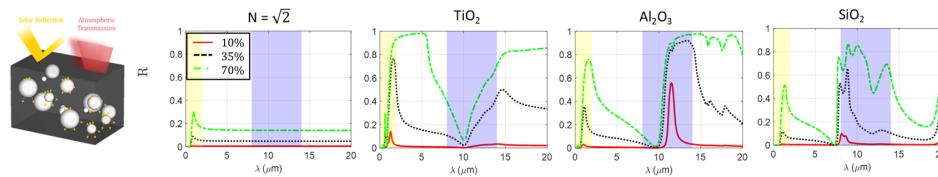


Fig. 3. Calculated reflectivity for a composite material consisting of an air host medium containing a random distribution of nanoparticles made of (a) a nondispersive dielectric material ($\epsilon_p = 2$), (b) titanium dioxide, (c) alumina and (d) silica, for different filling factors $f = 10\%$, 35% and 70% . The nanoparticles size distribution ranges from 50 nm to 300 nm radius, with a step of 50 nm. Yellow and blue region correspond to the solar and atmospheric window, respectively.

It is found that composites made of TiO_2 and Al_2O_3 act as very selective materials, exhibiting a high reflectivity at wavelengths shorter and longer than that of the suppressed-scattering window. Again, material dispersion is key for understanding the overall response of the composite. At wavelengths shorter than the suppressed-scattering window, high reflectivity is obtained via Mie-scattering resonances. At longer wavelengths, high reflectivity is associated with the negative value of the nanoparticles permittivity (see Fig. 2(a)), effectively acting as a nonresonant and homogeneous mirror. Thus, our results demonstrate that by exploiting material dispersion it is possible to design highly-reflective composite materials, which nevertheless remain transparent in a selective window.

4. Extension to metasurfaces and different nanoparticle shapes

Since suppressed-scattering windows are solely induced by the material properties of the nanoparticles, their existence should be guaranteed independently of the geometry of the system. Therefore, suppressed-scattering windows should be observed irrespectively of the shape (cylindrical, elliptical or arbitrary) and/or the arrangement (metasurfaces, photonic crystals, metamaterials) of the nanoparticles. To illustrate this point, Fig. 4 depicts the reflectivity of a metasurface consisting of a hexagonal array of small truncated cylinders. The aspect ratio of the cylinders, $AR = \text{height } (H) / \text{diameter } (D)$, is set to $AR = 1$, and period of the arrays is set to $P = 3/2 \cdot D$. In order to assess the geometry-independence of suppressed-scattering windows, the diameter of the cylinders is varied from $D = 2 \mu\text{m}$ to $D = 6 \mu\text{m}$. The results were obtained with a full-wave numerical solver (see Methods: Numerical calculations). The calculated reflectivities are characterized by a discrete spectrum with multiple resonant peaks, consistent with the periodic nature of the geometry. In general, the positioning of the resonances critically depends on the size of the truncated cylinders.

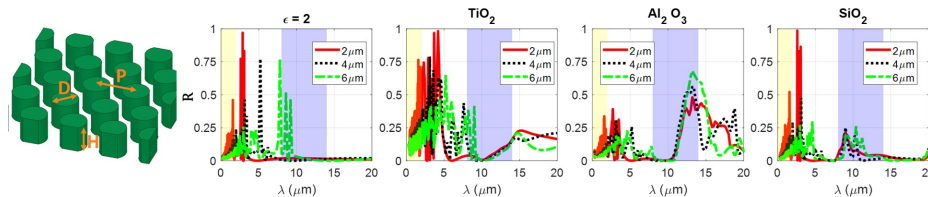


Fig. 4. Calculated reflectivity for a metasurface consisting of an hexagonal array of truncated cylinders made of (a) a nondispersive dielectric material ($\epsilon_p = 2$), (b) titanium dioxide, (c) alumina and (d) silica, for different cylinder diameters. Yellow and blue region correspond to the solar and atmospheric window, respectively.

However, it is observed that, for the arrays of TiO_2 , Al_2O_3 and SiO_2 dispersive cylinders, the reflectivity is consistently suppressed at wavelengths corresponding to minima of the scattering of individual particles (see Fig. 2). Moreover, this effect takes place independently of the geometrical configuration of the metasurfaces, i.e., changes in the diameter of the rods. Therefore, the numerical simulations demonstrate that our results can be extended to particles of arbitrary shape, as well as to regular arrangements. Thus, suppressed-scattering windows open the possibility of designing metasurfaces with strong resonance effects at specific wavelengths, while ensuring the existence of a fixed transparency band. We expect that many of the applications of Mie-resonant metaphotonics / Mie-tronics [55,56] might benefit from this simple design principle. Materials like TiO_2 and Al_2O_3 , whose suppressed-scattering windows overlap the atmospheric transparency window, seem particularly suitable not only for radiative cooling, but for any radiative thermal engineering applications.

5. From dispersive nanoparticles to dispersive hosts

Up to this point, our analysis has focused on dispersive nanoparticles embedded in a nondispersive host. However, it is expected that a co-design of nanoparticle and host material dispersion will be needed in many practical cases. Here we investigate the scattering performance of nanoparticles embedded in a dispersive calcium-silicate-hydrate (CSH) host. CSH is of great technological interest as it is the main phase of concrete, thus with the potential to critically impact the practical deployment of radiative cooling systems. The permittivity of CSH is depicted in Fig. 5 as computed from atomistic simulations (see Methods: Material parameters). It can be concluded from the figure that CSH behaves as a nearly-nondispersive dielectric at visible frequencies, while

it features several material resonances within the atmospheric window. Therefore, CSH is a good thermal emitter, but its reduced solar reflectance limits its applicability for daylight operation.

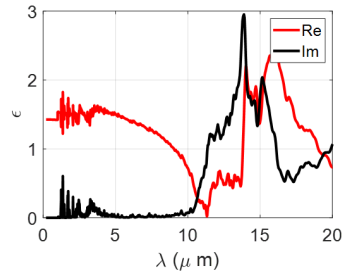


Fig. 5. Frequency dispersion of the permittivity of CSH.

However, the solar reflectivity of CSH can be enhanced by adding resonant nanoparticles and/or by controlling its internal porosity. Figure 6 shows the scattering efficiency spectra as a function of the nanoparticle radii for nondispersive ($\epsilon_p = 2$), TiO_2 , Al_2O_3 and SiO_2 nanoparticles immersed in a CSH host. As expected, the dispersion of the host material impacts the scattering efficiency, and, in particular, the existence of suppressed-scattering windows. For example, nondispersive nanoparticles do not exhibit any suppressed-scattering window when immersed in air (see Fig. 2), but they are shown to exhibit a suppressed-scattering window at long wavelengths when immersed in CSH. Furthermore, the frequency positioning and the depth of the suppressed-scattering windows of Al_2O_3 , TiO_2 and SiO_2 nanoparticles are affected by the dispersion of CSH. Specifically, the suppressed-scattering window of SiO_2 is shifted to shorter wavelengths, and a second window appears at longer wavelengths. Similarly, the suppressed-scattering window of TiO_2 is shifted, and features a smaller depth. On the contrary, the suppressed-scattering window of Al_2O_3 retains a considerable depth for all the studied radii, suggesting that it might be the best candidate to enhance the radiative cooling performance of CSH. In general, our results highlight the need of codesigning the material dispersion of nanoparticles and host in order to achieve the best performance.

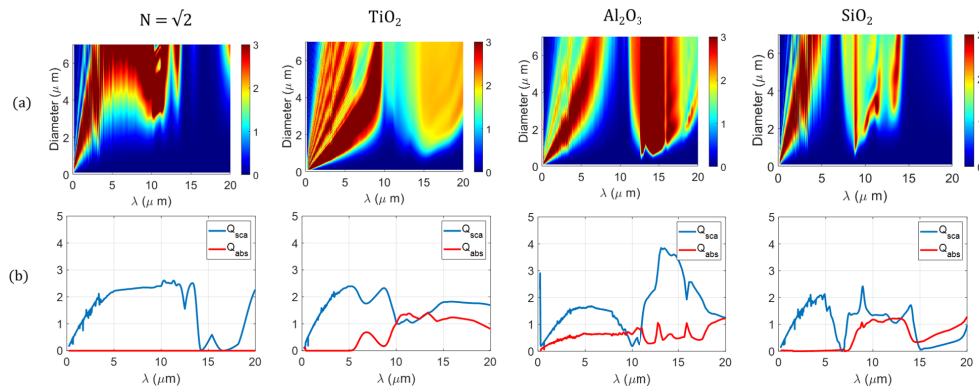


Fig. 6. (a) Scattering efficiency Q_{sca} calculations for nondispersive dielectric ($\epsilon_p = 2$), titanium dioxide (TiO_2), alumina (Al_2O_3), and silica (SiO_2) nanoparticles, embedded in a CSH host. (c) Average value of the scattering and absorption efficiencies for nanoparticle radii from 0 to $7\mu m$.

Finally, we investigate the scattering performance of air ($\epsilon_p = 1$) bubbles of different size within a host CSH material, modeling nanoporous in CSH. The scattering efficiency, presented

in Fig. 7, reveals that the porosity introduces Mie resonances in the visible, with the potential to enhance the solar reflectivity. At the same time, CSH porosity is found to exhibit a suppressed-scattering windows around $9\ \mu\text{m}$, allowing for selective thermal emission in the atmospheric window. Therefore, CSH porosity has the key ingredients to boost radiative cooling performance, and controlled nanoporosity might open a pathway for efficient concrete-based daylight radiative cooling.

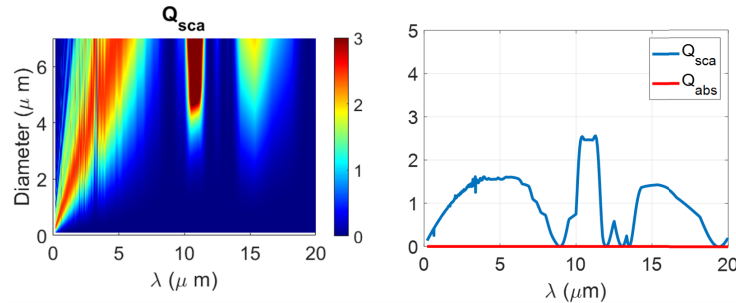


Fig. 7. (a) Scattering efficiency Q_{sca} calculations for porosity bubbles ($\epsilon_p = 1$) embedded in a CSH host. and (b) Average value of the scattering and absorption efficiencies.

Nanometer-scale length of cement-based materials is dominated by the so-called colloidal-scale porosity within CSH gel phases [57,58] (i.e., arising from the colloidal particle dispersion in porous media [59]). It is known that nanoporosity can have huge effects on the overall thermo-physical and mechanical properties of cement systems [60–62]. Our results demonstrate that nanoporosity will also have a profound impact on their radiative cooling performance. Multiple studies have been proposed to tune the inner pore structures and to sharpen the performance of cement-based materials by employing supplementary materials such as reactive slags or by products like clay, metakaolin, silica fume, fly ash, graphene oxides, colloidal nano-silica, carbon nanofibers and nanotubes, etc. [63–66]. Our results suggest that the impact of such tuning on the radiative cooling performance should be addressed, simultaneously optimizing optical material dispersion and scattering performance, and the thermal and chemical properties of cement systems.

6. Conclusions

We studied the scattering performance of popular nanoparticles employed to enhance the solar reflectance for radiative cooling applications, including ideally nondispersive nanoparticles, and nanoparticles made of popular materials in radiative cooling applications. All the studied nanoparticles approximately behave as nondispersive dielectrics in the visible, allowing for an improvement of the solar reflectance via Mie resonances. However, their response at infrared frequencies is found to be qualitatively different, highlighting the need to take into account the frequency dispersion. We found that alumina (Al_2O_3), and titanium dioxide (TiO_2) nanoparticles exhibit suppressed-scattering windows overlapping with the atmospheric window, while silica (SiO_2) nanoparticles exhibit strong resonances in the same frequency range. In turn, those differences lead to different design strategies for radiative coolers. It was shown that suppressed-scattering windows result in robust and selective transmissive bands within a highly reflecting window. Our results highlight a key insight in the design of selective thermal emitters for radiative cooling applications, and it can be applied in a variety of materials and technological platforms.

We used a generalized Maxwell-Garnett theory to demonstrate that our conclusions extend to random mixtures of nanoparticles. We expect that the intuitions obtained from scattering theory will provide helpful design guidelines for composite materials. We also used numerical

simulations to demonstrate that the concept of a suppressed-scattering windows can be applied to metasurfaces and other regular structures. The possibility of fixing a transparency window while independently tuning resonant effects at other wavelengths might find applications in Mie-resonant metaphotonics.

Finally, we analyzed the scattering performance of the porosity (air bubbles) of CSH, acting as a dispersive host. Our analysis reveals that the porosity of CSH gathers the key ingredients for daylight passive radiative cooling operation. Since CSH is the main phase of concrete, our results motivate further research on the control of nanoporosity of concrete, with the potential to enable a mass deployment of daylight radiative cooling applications.

Appendix: Materials and methods

Material parameters

The frequency dependence of the permittivity of titanium dioxide (TiO_2), alumina (Al_2O_3) and silicon dioxide (SiO_2) were obtained from tabulated data [67–72]. For the nondispersive dielectric, $\epsilon_p = 2$ was assumed at all frequencies. The dispersive permittivity of CSH was obtained from atomistic simulations. First, the crystalline structure of CSH was determined following [73]. The permittivity tensor components can be written as a function of the atomic vibrations (phonons) as

$$\epsilon_{ij}(\omega) = \epsilon_{ij}(\infty) + \frac{4\pi}{V} \sum_m \frac{\Omega_{ij}^m}{\omega_m^2 - \omega^2} \quad (1)$$

with frequency ω_m and the intensity oscillator tensor Ω_{ij}^m , which depends on the effective Born charge (q_B) and the eigenvector (e_{ij}) of the mode as

$$\Omega_{\alpha\beta} = \left(\sum_i \frac{q_{i\alpha j}^B e_{ij}}{m_i^{1/2}} \right) \left(\sum_i \frac{q_{i\beta j}^B e_{ij}}{m_i^{1/2}} \right) \quad (2)$$

Simulations for the vibrational modes were carried out with the software package GULP [74], using a polarizable force field that has been previously used for cement-based materials in the THz range [75]. Singularities were avoided by adding a damping term δ of 0.15 THz, i.e., $\omega^2 = \omega(\omega + i\delta)$. Finally, an isotropic permittivity is approximated by averaging the diagonal terms, i.e., $\epsilon_h = \epsilon_{xx} + \epsilon_{yy} + \epsilon_{zz}$.

Calculation of the scattering efficiency

Scattering efficiencies were computed by using Mie theory [76]. The scattering efficiency is defined as the scattering cross section normalized to the area of the particle

$$Q_{sca} = \frac{C_{sca}}{\pi a^2} \quad (3)$$

where a is the nanoparticle radius, and C_{csa} is the scattering cross-section

$$C_{sca} = \frac{2\pi}{k^2} \sum_{n=1}^{\infty} (2n+1)(|a_n|^2 + |b_n|^2) \quad (4)$$

with $k = \omega/c\sqrt{\epsilon_h}$ being the propagation constant in a host with permittivity ϵ_h . a_n and b_n are the scattering coefficients

$$a_n = \frac{m\Psi_n(mx)\Psi'_n(x) - \Psi(x)\Psi'(mx)}{m\Psi_n(mx)\xi'_n(x) - \xi_n(x)\Psi'_n(mx)} \quad (5)$$

$$b_n = \frac{\Psi_n(mx)\Psi'_n(x) - m\Psi(x)\Psi'(mx)}{\Psi_n(mx)\xi'_n(x) - m\xi_n(x)\Psi'_n(mx)} \quad (6)$$

where $m = \sqrt{\varepsilon_p/\varepsilon_h}$ is the refractive index ratio, $x = ka$ is the size parameter, $\Psi_n(x)$ is the spherical Bessel function of the first kind and order n , $\xi_n(x)$ is the spherical Hankel function of the first kind and order n , and $f'_n(x) = df_n(x)/dx$, $f = \Psi, \xi$.

Calculation of the reflectivity from composite materials

The reflectivity at normal incidence from a composite material with effective permittivity ε_e and effective permeability μ_e is given by [77]

$$R = \left| \frac{1 - \sqrt{\varepsilon_e/\mu_e}}{1 + \sqrt{\varepsilon_e/\mu_e}} \right|^2 \quad (7)$$

Following generalized Maxwell-Garnett rules, ε_e and μ_e can be directly linked to the scattering properties of individual nanoparticles and the filling factor f as follows [52,53]

$$\varepsilon_e = \varepsilon_h \frac{1 + 2\gamma/3}{1 - \gamma/3} \quad (8)$$

$$\mu_e = \frac{1 + 2\delta/3}{1 - \delta/3} \quad (9)$$

with

$$\gamma = \sum_{i=1}^M j \frac{3f_i}{2(ka_i)^3} (S_{1i}(0) + S_{1i}(\pi)) \quad (10)$$

$$\delta = \sum_{i=1}^M j \frac{3f_i}{2(ka_i)^3} (S_{1i}(0) - S_{1i}(\pi)) \quad (11)$$

where M is the length of the particle size vector, $f_i = f/M$ is the individual filling factor for a uniform size distribution and f is the overall filling factor. $S_{1i}(\theta)$ is angle-dependent scattering amplitude associated with particle size a_i :

$$S_{1i}(\theta) = \sum_{n=1}^{\infty} \frac{2n+1}{n(n+1)} \left[a_{ni} \frac{P_n^1(\cos \theta)}{\sin \theta} + b_{ni} \frac{\partial}{\partial \theta} P_n^1(\cos \theta) \right] \quad (12)$$

where P_n^1 is the associate Legendre polynomial of order n and degree $l = 1$, and a_{ni} and b_{ni} are the scattering coefficient associated to the element i of the particle size distribution, which encapsulate the material properties of the particles, such as its permittivity ε_p .

Numerical simulations

Reflection from a metasurface, consisting of a regular array of truncated cylinders, was numerically obtained by using the Grating Diffraction Calculator (GD-Calc) MATLAB-based software for diffraction grating simulation using rigorous coupled-wave (RCW) theory [78,79]. For this numerical analysis normal incidence is considered and the reflectance is calculated as the average of the reflectances obtained with two orthogonal linear polarization states.

Funding. HORIZON EUROPE Framework Programme (964450, MIRACLE).

Acknowledgments. The authors acknowledge financial support from European Union's Horizon 2020 research and innovation program under grant agreement 964450, MIRACLE.

Disclosures. The authors declare no conflicts of interest.

Data availability. Data underlying the results presented in this paper are not publicly available at this time but may be obtained from the authors upon reasonable request.

References

1. S. Fan and W. Li, "Photonics and thermodynamics concepts in radiative cooling," *Nat. Photonics* **16**(3), 182–190 (2022).
2. M. M. Hossain and M. Gu, "Radiative cooling: principles, progress, and potentials," *Adv. Sci.* **3**(7), 1500360 (2016).
3. D. Zhao, A. Aili, Y. Zhai, S. Xu, G. Tan, X. Yin, and R. Yang, "Radiative sky cooling: Fundamental principles, materials, and applications," *Appl. Phys. Rev.* **6**(2), 021306 (2019).
4. X. Yin, R. Yang, G. Tan, and S. Fan, "Terrestrial radiative cooling: Using the cold universe as a renewable and sustainable energy source," *Science* **370**(6518), 786–791 (2020).
5. A. P. Raman, M. A. Anoma, L. Zhu, E. Rephaeli, and S. Fan, "Passive radiative cooling below ambient air temperature under direct sunlight," *Nature* **515**(7528), 540–544 (2014).
6. M. Zeyghami, D. Y. Goswami, and E. Stefanakos, "A review of clear sky radiative cooling developments and applications in renewable power systems and passive building cooling," *Sol. Energy Mater. Sol. Cells* **178**, 115–128 (2018).
7. N. Cunha, A. Al-Rjoub, L. Rebouta, L. Vieira, and S. Lanceros-Mendez, "Multilayer passive radiative selective cooling coating based on $\text{Al}/\text{SiO}_2/\text{SiNx}/\text{SiO}_2/\text{TiO}_2/\text{SiO}_2$ prepared by dc magnetron sputtering," *Thin Solid Films* **694**, 137736 (2020).
8. M. A. Kecebas, M. P. Menguc, A. Kosar, and K. Sendur, "Spectrally selective filter design for passive radiative cooling," *J. Opt. Soc. Am. B* **37**(4), 1173–1182 (2020).
9. Z. F. Mira, S.-Y. Heo, G. J. Lee, and Y. M. Song, "Multilayer selective passive daytime radiative cooler optimization utilizing memetic algorithm," *J. Quant. Spectrosc. Radiat. Transf.* **272**, 107774 (2021).
10. G. Mabchour, M. Benlattar, K. Saadouni, and M. Mazroui, "Daytime radiative cooling purposes with selective multilayer design based on Ta_2O_5 ," *Optik* **214**, 164811 (2020).
11. M. M. Hossain, B. Jia, and M. Gu, "A metamaterial emitter for highly efficient radiative cooling," *Adv. Opt. Mater.* **3**(8), 1047–1051 (2015).
12. A. K. Goyal and A. Kumar, "Recent advances and progresses in photonic devices for passive radiative cooling application: a review," *J. Nanophotonics* **14**(03), 030901 (2020).
13. S. Atiganyanun, J. B. Plumley, S. J. Han, K. Hsu, J. Cytrynbaum, T. L. Peng, S. M. Han, and S. E. Han, "Effective radiative cooling by paint-format microsphere-based photonic random media," *ACS Photonics* **5**(4), 1181–1187 (2018).
14. X. Li, J. Peoples, P. Yao, and X. Ruan, "Ultrawhite baso4 paints and films for remarkable daytime subambient radiative cooling," *ACS Appl. Mater. Interfaces* **13**(18), 21733–21739 (2021).
15. Z. Cheng, F. Wang, H. Wang, H. Liang, and L. Ma, "Effect of embedded polydisperse glass microspheres on radiative cooling of a coating," *Int. J. Therm. Sci.* **140**, 358–367 (2019).
16. Z. Huang and X. Ruan, "Nanoparticle embedded double-layer coating for daytime radiative cooling," *Int. J. Heat Mass Transfer* **104**, 890–896 (2017).
17. A. R. Gentle and G. B. Smith, "Radiative heat pumping from the earth using surface phonon resonant nanoparticles," *Nano Lett.* **10**(2), 373–379 (2010).
18. Y. Zhai, Y. Ma, S. N. David, D. Zhao, R. Lou, G. Tan, R. Yang, and X. Yin, "Scalable-manufactured randomized glass-polymer hybrid metamaterial for daytime radiative cooling," *Science* **355**(6329), 1062–1066 (2017).
19. J. Mandal, Y. Fu, A. C. Overvig, M. Jia, K. Sun, N. N. Shi, H. Zhou, X. Xiao, N. Yu, and Y. Yang, "Hierarchically porous polymer coatings for highly efficient passive daytime radiative cooling," *Science* **362**(6412), 315–319 (2018).
20. D. Li, X. Liu, W. Li, Z. Lin, B. Zhu, Z. Li, J. Li, B. Li, S. Fan, J. Xie, and J. Zu, "Scalable and hierarchically designed polymer film as a selective thermal emitter for high-performance all-day radiative cooling," *Nat. Nanotechnol.* **16**(2), 153–158 (2021).
21. Y. Gao, X. Song, A. S. Farooq, and P. Zhang, "Cooling performance of porous polymer radiative coating under different environmental conditions throughout all-year," *Sol. Energy* **228**, 474–485 (2021).
22. N. N. Shi, C.-C. Tsai, M. J. Carter, J. Mandal, A. C. Overvig, M. Y. Sfeir, M. Lu, C. L. Craig, G. D. Bernard, Y. Yang, and N. Yu, "Nanostructured fibers as a versatile photonic platform: radiative cooling and waveguiding through transverse anderson localization," *Light: Sci. Appl.* **7**(1), 37 (2018).
23. N. N. Shi, C.-C. Tsai, F. Camino, G. D. Bernard, N. Yu, and R. Wehner, "Keeping cool: Enhanced optical reflection and radiative heat dissipation in saharan silver ants," *Science* **349**(6245), 298–301 (2015).
24. S. Zeng, S. Pian, and M. Su, *et al.*, "Hierarchical-morphology metafabric for scalable passive daytime radiative cooling," *Science* **373**(6555), 692–696 (2021).
25. B. Zhu, W. Li, Q. Zhang, D. Li, X. Liu, Y. Wang, N. Xu, Z. Wu, J. Li, X. Li, P. B. Catrysse, W. Xu, S. Fan, and J. Zhu, "Subambient daytime radiative cooling textile based on nanoprocessed silk," *Nat. Nanotechnol.* **16**(12), 1342–1348 (2021).
26. T. Li, Y. Zhai, S. He, W. Gan, Z. Wei, M. Heidarnejad, D. Dalgo, R. Mi, X. Zhao, J. Song, J. Dai, C. Chen, A. Aili, A. Vellore, A. Martini, R. Yang, J. Srebric, X. Yin, and L. Hu, "A radiative cooling structural material," *Science* **364**(6442), 760–763 (2019).
27. Z. Ruan and S. Fan, "Superscattering of light from subwavelength nanostructures," *Phys. Rev. Lett.* **105**(1), 013901 (2010).
28. A. Krasnok, D. Baranov, H. Li, M.-A. Miri, F. Monticone, and A. Alú, "Anomalies in light scattering," *Adv. Opt. Photonics* **11**(4), 892–951 (2019).

29. I. Liberal, I. Ederra, R. Gonzalo, and R. W. Ziolkowski, "Upper bounds on scattering processes and metamaterial-inspired structures that reach them," *IEEE Trans. Antennas Propag.* **62**(12), 6344–6353 (2014).
30. A. Alù and N. Engheta, "Achieving transparency with plasmonic and metamaterial coatings," *Phys. Rev. E* **72**(1), 016623 (2005).
31. S. Arslanagić and R. W. Ziolkowski, "Highly subwavelength, superdirective cylindrical nanoantenna," *Phys. Rev. Lett.* **120**(23), 237401 (2018).
32. R. W. Ziolkowski, "Using Huygens multipole arrays to realize unidirectional needle-like radiation," *Phys. Rev. X* **7**(3), 031017 (2017).
33. A. Alù and N. Engheta, "Cloaking a sensor," *Phys. Rev. Lett.* **102**(23), 233901 (2009).
34. I. Liberal and R. W. Ziolkowski, "Analytical and equivalent circuit models to elucidate power balance in scattering problems," *IEEE Trans. Antennas Propag.* **61**(5), 2714–2726 (2013).
35. I. Liberal, I. Ederra, R. Gonzalo, and R. W. Ziolkowski, "Superbackscattering from single dielectric particles," *J. Opt.* **17**(7), 072001 (2015).
36. A. W. Powell, A. P. Hibbins, and J. R. Sambles, "Multiband superbackscattering via mode superposition in a single dielectric particle," *Appl. Phys. Lett.* **118**(25), 251107 (2021).
37. I. Liberal, I. Ederra, R. Gonzalo, and R. W. Ziolkowski, "Superbackscattering antenna arrays," *IEEE Trans. Antennas Propag.* **63**(5), 2011–2021 (2015).
38. F. Monticone, C. Argyropoulos, and A. Alù, "Multilayered plasmonic covers for comblike scattering response and optical tagging," *Phys. Rev. Lett.* **110**(11), 113901 (2013).
39. M. F. Limonov, M. V. Rybin, A. N. Poddubny, and Y. S. Kivshar, "Fano resonances in photonics," *Nat. Photonics* **11**(9), 543–554 (2017).
40. I. Liberal and N. Engheta, "Nonradiating and radiating modes excited by quantum emitters in open epsilon-near-zero cavities," *Sci. Adv.* **2**(10), e1600987 (2016).
41. F. Monticone and A. Alu, "Embedded photonic eigenvalues in 3d nanostructures," *Phys. Rev. Lett.* **112**(21), 213903 (2014).
42. M. G. Silveirinha, "Trapping light in open plasmonic nanostructures," *Phys. Rev. A* **89**(2), 023813 (2014).
43. A. E. Miroshnichenko, A. B. Evlyukhin, Y. F. Yu, R. M. Bakker, A. Chipouline, A. I. Kuznetsov, B. Luk'yanchuk, B. N. Chichkov, and Y. S. Kivshar, "Nonradiating anapole modes in dielectric nanoparticles," *Nat. Commun.* **6**(1), 8069 (2015).
44. P. Bharadwaj, B. Deutsch, and L. Novotny, "Optical antennas," *Adv. Opt. Photonics* **1**(3), 438–483 (2009).
45. P. Lodahl, S. Mahmoodian, and S. Stobbe, "Interfacing single photons and single quantum dots with photonic nanostructures," *Rev. Mod. Phys.* **87**(2), 347–400 (2015).
46. E. Yablonovitch, "Inhibited spontaneous emission in solid-state physics and electronics," *Phys. Rev. Lett.* **58**(20), 2059–2062 (1987).
47. S. Arslanagić and R. W. Ziolkowski, "Jamming of quantum emitters by active coated nanoparticles," *IEEE J. Sel. Top. Quantum Electron.* **19**(3), 4800506 (2013).
48. T. Gong, I. Liberal, M. Camacho, B. Spreng, N. Engheta, and J. N. Munday, "Radiative energy bandgap of nanostructures coupled with quantum emitters around the epsilon-near-zero (ENZ) frequency," *arXiv preprint arXiv:2203.02062* (2022).
49. W. Li, Y. Li, and K. W. Shah, "A materials perspective on radiative cooling structures for buildings," *Sol. Energy* **207**, 247–269 (2020).
50. J. Liu, Z. Zhou, J. Zhang, W. Feng, and J. Zuo, "Advances and challenges in commercializing radiative cooling," *Mater. Today Phys.* **11**, 100161 (2019).
51. A. H. Sihvola, *Electromagnetic Mixing Formulas and Applications*, 47 (IET, 1999).
52. J. P. Bijarniya, J. Sarkar, and P. Maiti, "Review on passive daytime radiative cooling: Fundamentals, recent researches, challenges and opportunities," *Renew. Sustain. Energy Rev.* **133**, 110263 (2020).
53. G. A. Niklasson and T. S. Eriksson, "Radiative cooling with pigmented polyethylene foils," in *Optical Materials Technology for Energy Efficiency and Solar Energy Conversion VII*, vol. 1016 (SPIE, 1989), pp. 89–99.
54. C. F. Bohren, "Applicability of effective-medium theories to problems of scattering and absorption by nonhomogeneous atmospheric particles," *J. Atmos. Sci.* **43**(5), 468–475 (1986).
55. A. I. Kuznetsov, A. E. Miroshnichenko, M. L. Brongersma, Y. S. Kivshar, and B. Luk'yanchuk, "Optically resonant dielectric nanostructures," *Science* **354**(6314), aag2472 (2016).
56. K. Koshelev and Y. Kivshar, "Dielectric resonant metaphotonics," *ACS Photonics* **8**(1), 102–112 (2021).
57. H. M. Jennings, J. J. Thomas, J. S. Gevrenov, G. Constantinides, and F.-J. Ulm, "A multi-technique investigation of the nanoporosity of cement paste," *Cem. Concr. Res.* **37**(3), 329–336 (2007).
58. X. Zhang, H. Yang, Q. Yang, X. Du, C. Li, and X. Cheng, "Effects of particle size of colloidal nanosilica on hydration of portland cement at early age," *Adv. Mech. Eng.* **11**(2), 1687814019828948 (2019).
59. P. R. Johnson, N. Sun, and M. Elimelech, "Colloid transport in geochemically heterogeneous porous media: Modeling and measurements," *Environ. Sci. Technol.* **30**(11), 3284–3293 (1996).
60. H. M. Jennings, J. W. Bullard, J. J. Thomas, J. E. Andrade, J. J. Chen, and G. W. Scherer, "Characterization and modeling of pores and surfaces in cement paste: correlations to processing and properties," *J. Adv. Concr. Technol.* **6**(1), 5–29 (2008).

61. A. J. Allen, J. J. Thomas, and H. M. Jennings, "Composition and density of nanoscale calcium–silicate–hydrate in cement," *Nat. Mater.* **6**(4), 311–316 (2007).
62. M. Azimi-Pour and H. Eskandari-Naddaf, "Synergistic effect of colloidal nano and micro-silica on the microstructure and mechanical properties of mortar using full factorial design," *Constr. Build. Mater.* **261**, 120497 (2020).
63. S. Barbhuiya and P. Chow, "Nanoscaled mechanical properties of cement composites reinforced with carbon nanofibers," *Materials* **10**(6), 662 (2017).
64. M. Jafarbeglou, M. Abdouss, and A. A. Ramezani-pour, "Nanoscience and nano engineering in concrete advances, a review," *International Journal of Nanoscience and Nanotechnology* **11**, 263–273 (2015).
65. E. Horszczaruk, E. Mijowska, R. J. Kalenczuk, M. Aleksandrak, and S. Mijowska, "Nanocomposite of cement/graphene oxide–impact on hydration kinetics and young's modulus," *Constr. Build. Mater.* **78**, 234–242 (2015).
66. Z. Luo, W. Li, Y. Gan, X. He, A. Castel, and D. Sheng, "Nanoindentation on micromechanical properties and microstructure of geopolymer with nano-SiO₂ and nano-TiO₂," *Cem. Concr. Compos.* **117**, 103883 (2021).
67. M. Query, "Optical constants, contractor report," U.S. Army Chemical Research, Development and Engineering Center (CRDC), Aberdeen Proving Ground, MD **418**, 1 (1985).
68. I. H. Malitson, "Interspecimen comparison of the refractive index of fused silica," *J. Opt. Soc. Am.* **55**(10), 1205–1209 (1965).
69. C. Tan, "Determination of refractive index of silica glass for infrared wavelengths by ir spectroscopy," *J. Non-Cryst. Solids* **223**(1-2), 158–163 (1998).
70. R. Kitamura, L. Pilon, and M. Jonasz, "Optical constants of silica glass from extreme ultraviolet to far infrared at near room temperature," *Appl. Opt.* **46**(33), 8118–8133 (2007).
71. J. R. DeVore, "Refractive indices of rutile and sphalerite," *J. Opt. Soc. Am.* **41**(6), 416–419 (1951).
72. T. Siefke, S. Kroker, K. Pfeiffer, O. Puffky, K. Dietrich, D. Franta, I. Ohlídal, A. Szeghalmi, E.-B. Kley, and A. Tünnermann, "Materials pushing the application limits of wire grid polarizers further into the deep ultraviolet spectral range," *Adv. Opt. Mater.* **4**(11), 1780–1786 (2016).
73. E. Duque Redondo, "Atomistic simulations of confined species in 2d nanostructures: Clays and c-s-h gel," (2018).
74. J. D. Gale, "Gulp: A computer program for the symmetry-adapted simulation of solids," *J. Chem. Soc. Faraday Trans.* **93**(4), 629–637 (1997).
75. J. S. Dolado, G. Goracci, E. Duque, P. Martauz, Y. Zuo, and G. Ye, "Thz fingerprints of cement-based materials," *Materials* **13**(18), 4194 (2020).
76. C. F. Bohren and D. R. Huffman, *Absorption and Scattering of Light by Small Particles* (John Wiley & Sons, 2008).
77. C. A. Balanis, *Advanced Engineering Electromagnetics* (John Wiley & Sons, 2012).
78. C. Johnson Kenneth, "Grating diffraction calculator (gd-calc) [source code]."
79. https://www.mathworks.com/products/connections/product_detail/gd-calc.html, accessed Sept. 9, 2022.